Non-coding RNA Research 12 (2025) 20–33

Contents lists available at ScienceDirect

Non-coding RNA Research

journal homepage: www.keaipublishing.com/en/journals/non-coding-rna-research

Original Research Article

miR-210 overexpression increases pressure overload-induced cardiac fibrosis

G. Zaccagnini [a,b,*], D. Baci [a], S. Tastsoglou [a], I. Cozza [a], A. Madè [a], C. Voellenkle [a,b], M. Nicoletti [a], C. Ruatti [a], M. Longo [a], L. Perani [c], C. Gaetano [d], A. Esposito [c,e], F. Martelli [a,b,**]

[a] Laboratory of Molecular Cardiology, IRCCS Policlinico San Donato, San Donato Milanese, Milan, 20097, Italy
[b] Laboratory of Stem Cell Biology, Institute of Cellular Biology and Pathology "Nicolae Simionescu", Bucharest, Romania
[c] Preclinical Imaging Facility, Experimental Imaging Center, IRCCS San Raffaele Scientific Institute, Milan, 20132, Italy
[d] Laboratorio di Epigenetica, Istituti Clinici Scientifici Maugeri IRCCS, Pavia, 27100, Italy
[e] Vita-Salute San Raffaele University, Milan, 20132, Italy

ARTICLE INFO

Keywords:
miR-210
Pressure overload
Aortic stenosis
Inflammation
Fibrosis

ABSTRACT

Aortic stenosis, a common valvular heart disease, can lead to left ventricular pressure overload, triggering pro-fibrotic responses in the heart. miR-210 is a microRNA that responds to hypoxia and ischemia and plays a role in immune regulation and in cardiac remodeling upon myocardial infarction. This study investigated the effects of miR-210 on cardiac fibrosis caused by pressure overload.

Using a mouse model with inducible miR-210 over-expression, we subjected mice to transverse aortic constriction (TAC) to induce pressure overload. Mice with miR-210 over-expression developed eccentric hypertrophy, heightened expression of hypertrophic markers (Nppa and Nppb) and increased cross sectional area of cardiomyocytes, impacting the free wall of the left ventricle. These findings suggest that miR-210 worsens cardiac dysfunction. Furthermore, miR-210 over-expression led to a more robust and sustained inflammatory response in the heart, increased interstitial and perivascular fibrosis, and activation of myofibroblasts. miR-210 also promoted angiogenesis. *In vitro*, cardiac fibroblasts over-expressing miR-210 showed increased adhesion, wound healing and migration capacity.

Our results demonstrate that miR-210 contributes to adverse cardiac remodeling in response to pressure overload, including eccentric hypertrophy, inflammation, and fibrosis.

1. Introduction

Aortic stenosis (AS) is the most common valvular heart disease in Europe and North America, requiring a surgical or interventional treatment [1]. The prevalence of AS increases with aging, with an incidence averaging 9.8 % in 80–89 year-old patients [1–3]. AS is mainly due to calcification of the aortic valve, but it could also have rheumatic origins, or it could be due to congenital malformations of the valve. Calcific AS causes increased leaflet stiffness and narrowing of the valve orifice, resulting in left ventricular pressure overload [3]. Pressure overload, in turn, causes interstitial and perivascular fibrosis and leads to diastolic dysfunction that frequently progresses to ventricular dilation and combined diastolic and systolic heart failure [4,5]. Indeed, the mechanical stress due to pressure overload activates pro-fibrotic pathways that involve many cell types, particularly monocytes and macrophages, fibroblasts and cardiomyocytes. Monocytes and macrophages are pivotal in regulating fibrotic responses in many tissues [6]. Several experimental findings obtained in mouse models of pressure overload, highlighted that inflammatory cells, and in particular monocytes and macrophages, are key regulators in cardiac remodeling and fibrosis, since they secrete a wide range of bioactive mediators, including cytokines and matricellular proteins [5,7–9]. Monocytes and macrophages are highly plastic cells, exhibit remarkable heterogeneity and can respond to growth factors, cytokines, and other mediators released in the local tissue microenvironment, assuming either a pro-inflammatory

Peer review under the responsibility of Editorial Board of Non-coding RNA Research.
* Corresponding author. Via Morandi, 30, San Donato Milanese, (MI), 20097, Italy.
** Corresponding author. Via Morandi, 30, San Donato Milanese, (MI), 20097, Italy.
E-mail addresses: germana.zaccagnini@grupposandonato.it (G. Zaccagnini), fabio.martelli@grupposandonato.it (F. Martelli).

https://doi.org/10.1016/j.ncrna.2025.01.009
Received 21 March 2024; Received in revised form 23 January 2025; Accepted 26 January 2025
Available online 31 January 2025

Abbreviations

AS	aortic stenosis
α-SMA	alpha-Smooth muscle actin
CSA	cross sectional area
CFs	cardiac fibroblasts
LV	left ventricle
TAC	transverse aortic constriction
Tg-210	inducible miR-210 transgenic mouse
Wt	wild-type

or an anti-inflammatory, pro-repair phenotypes [6,10]. In addition, mechanical stress, metabolic dysfunction and inflammatory cytokines may induce a fibrogenic program in cardiomyocytes, contributing to fibroblast activation [7]. Fibroblast activation and transdifferentiation into myofibroblasts, is the key cellular event that drives the fibrotic response in several pathological conditions associated with heart failure, including pressure overload [7,11,12]. Indeed, myofibroblasts express contractile proteins such as α-smooth muscle actin and synthesize matricellular proteins leading to fibrosis.

miR-210 is a microRNA expressed in response to hypoxia and ischemia which modulates several target genes involved in these processes [13]. Interestingly, miR-210 is upregulated in heart failure diabetic patients affected by dilated ischemic cardiomyopathy [14]. miR-210 modulates several processes activated in hypoxia response by targeting specific mRNAs. In particular, it represses mitochondrial metabolism, promoting the shift from mitochondrial respiration to glycolysis [15], inhibits apoptosis [16,17], stimulates angiogenesis [16], and supports stem-cell survival [18,19].

There is much evidence of the immune-modulatory function of miR-210. Indeed, it regulates T lymphocyte subsets in psoriasis [20], potentiates the tumor-promoting effects of myeloid-derived suppressor cells [21], inhibits the production of pro-inflammatory cytokines in LPS-stimulated macrophages [22] and inhibits the pro-inflammatory immune responses of leishmania-infected macrophages [23]. Interestingly, miR-210 upregulation in monocytes and macrophages has been observed in response to pathogen interaction in different mouse infection models [24]. In particular, miR-210 induction in macrophages, leads to a switch towards a pro-inflammatory M1 phenotype by repressing mitochondrial oxidative metabolism and promoting glycolysis. Overall, these studies highlighted that the role of miR-210 in the modulation of the inflammatory response could be very different and should be evaluated in each specific context.

Recently, we demonstrated a context-dependent regulation by miR-210 of the inflammatory response and fibrosis [25]. Indeed, when macrophages expressing high miR-210 levels infiltrate a wild-type ischemic tissue, they switch toward a pro-fibrotic phenotype, leading to impaired tissue repair, fibrosis, and dysfunctional angiogenesis [25].

The miR-210 role in the modulation of tissue fibrosis has also been demonstrated in different pathologies. Indeed, atrial myocyte-derived exosomal miR-210 promoted atrial fibroblast proliferation and collagen synthesis by inhibiting GPD1L, contributing to atrial fibrosis and atrial fibrillation [26]. In idiopathic pulmonary fibrosis, hypoxia induces miR-210 expression via HIF-2 alpha. miR-210 in turn drives fibroblasts proliferation, by repressing the c-myc inhibitor MNT, (MAX network transcriptional repressor), leading to pulmonary fibrosis [27]. Remarkably, miR-210 function, as for all micro-RNAs, depends on the target mRNAs expressed by each cell type and might be highly context- and time-dependent.

Finally, miR-210 has been proposed as a biomarker in AS, since circulating miR-210 levels are increased in patients with AS and provide independent prognostic information to established risk indices [28].

In this work, we investigated the role of miR-210 in tissue fibrosis following pressure overload in mice.

2. Materials and methods

Ethical statement

This study was approved by the Italian National Institute of Health and supervised by the Institutional Animal Care and Use Committee of San Raffaele Hospital (Milan). All experimental procedures complied with the Guidelines of the Italian National Institute of Health and with the *Guide for the Care and Use of Laboratory Animals* (Institute of Laboratory Animal Resources, National Academy of Sciences, Bethesda, Md).

2.1. Mouse model

Doxycycline-inducible transgenic C57BL/6NTac-*Gt(ROSA)26Sor*$^{tm3720(Mir210)Tac}$ male mice (Tg-210) and Wild-type littermates (Wt), as well as genotyping analysis were previously described [29]. For miR-210 induction, Wt and Tg-210 male mice, two months old, were fed with pellets of food containing Doxycycline (NFM18 diet added with doxycycline hyclate 2000 mg/kg, Mucedola, Italy) starting from 7 days before surgery and until the endpoint of the experiment. Doxycycline was administrated to Wt littermate too, in order to exclude side effects of the drug. The effectiveness of miR-210 induction was assessed by qRT-PCR on left ventricle (LV) or liver samples from each analyzed mouse. Before all surgical and perfusion procedures, mice were anesthetized with an intraperitoneal injection of 100 mg/kg ketamine (Ketavet 100; Intervet Farmaceutici, Italy) and medetomidine 0.5 mg/kg (Domitor, Orion Pharma, Italy). Transverse aortic constriction (TAC) was induced by a minimally invasive surgical procedure as previously described [30]. Briefly, a suprasternal skin incision was made, followed by a mini-proximal sternotomy. The thymus was retracted to expose the aortic arch, and the fat around the aortic arch was carefully removed. A surgical suture Prolene 8–0 (Ethicon, USA) was passed underneath the aorta between the origins of the brachiocephalic and left common carotid arteries. A bent 27-gauge needle was placed next to the aortic arch, and the suture was tightly tied around the needle and the aorta. After ligation, the needle was quickly removed. The sternum and the skin were closed, and mice were allowed to recover by an intraperitoneal injection of Atipamezole 5 mg/kg (Antisedan, Orion Pharma, Italy) and maintained under a warming infrared lamp until they were fully awake. The sham procedure was identical except that the aorta was not ligated. Ultrasound imaging was performed by an experienced operator using a high-performance ultrasonographic Imaging System (Vevo 2100; Fujifilm VisualSonics Inc., Toronto, ON, Canada). The aortic arch view was obtained from a modified right parasternal view on day 7 after surgery. PW Doppler Mode waveforms of the transverse aortic flow at the ligation level were acquired using a 21 MHz central frequency linear probe (MS-250, bandwidth 13–24 MHz, FUJIFILM VisualSonics Inc., Toronto, ON, Canada), lateral and axial resolution of 165 and 75 μm, respectively. The pressure gradient was estimated using the modified Bernoulli equation (pressure gradient = 4*velocity^2) to assess the presence of TAC. Transthoracic echocardiography was performed at 7 and 28 days after surgery. Two-dimensional short-axis images and M-mode tracings were recorded at the level of papillary muscles. From M-mode tracings, anatomical parameters in diastole and systole were obtained by Vevo Lab 3.2.6 software (Fujifilm VisualSonics Inc., Toronto, ON, Canada). The echocardiographic parameters obtained in Wt sham-operated mice at days 7 and 28 post-surgery were used as reference values. Before samples harvesting after 7 or 28 days of pressure overload, mice underwent euthanasia by cervical dislocation or anesthetic overdosing.

2.2. Experimental design

In order to induce miR-210 over-expression, mice were fed with food pellets containing doxycycline starting from 7 days before surgery and

until the experiment's endpoint.

At time 0, mice underwent Sham or TAC surgery. All mice underwent echocardiography on day 7 and were randomly assigned to two groups. The first group was sacrificed on day 7. The second group was analyzed at day 28 and sacrificed. Next, hearts were collected for further analysis (Supplementary Fig. S1).

2.3. Sample preparations

For RNA extraction, LVs were snap frozen in liquid nitrogen. For histological analysis, mice were perfused via LV with PBS pH 7.5, followed by 10 % buffered formalin (Bio-Optica, Italy), at 100 mm/Hg for 10 min. Subsequently, hearts were collected, fixed and paraffin-embedded and sections were prepared as previously described [31].

2.4. miRNA and mRNA quantification

Total RNA was extracted from cells and tissue using TRIzol (Thermo Fisher Scientific, MA, USA) and the TissueLyser system (Qiagen, Hilden, Germany). miRNA and mRNA levels were analyzed using the TaqMan qRT-PCR assay (miR-16 Assay ID 000391, U6 snRNA Assay ID 001973, miR-210 Assay ID 000512, Thermo Fisher Scientific, MA, USA) and the SYBR-GREEN qRT-PCR method (Promega, Madison, Wisconsin, USA) respectively, and quantified with the Step-One plus real-time PCR System (Thermo Fisher Scientific, MA, USA), as previously described [29]. Primers used for qRT-PCR are listed in Table S1 (Supplementary materials). miRNA and mRNA relative expression was calculated using the comparative Ct method (−Delta Delta Ct (-ΔΔCt)) [32] and the expression values were normalized to miR-16, U6 and RPL13 levels, that preliminary experiments indicated as not modulated by TAC or miR-210 (not shown).

2.5. Histology and morphometric analysis

2.5.1. Immunofluorescence staining

For immunofluorescence (IF) and immunohistochemistry (IHC) staining, the following antibodies were used: rat anti-Galectin-3 (Mac-2, #CL8942AP, Cedarlane Burlington, Canada), rabbit polyclonal anti-Laminin (#Z0097, Agilent Dako, USA), rabbit monoclonal anti-alpha-Smooth Muscle Actin (α-SMA) (#ab124964, Abcam, Cambridge, UK). Hoechst 33342 (#H3570, Thermo Fisher Scientific, MA, USA) was used for nuclei staining.

For all the quantification, two regions of interest (ROIs) were manually defined in specific areas of the LV: the septum and the free wall (Supplementary Fig. S2).

2.5.2. Quantification of Galectin-3 positive areas

Images of the whole section of the heart were acquired by Aperio AT2 digital scanner at magnification of 200× (Leica Biosystems, Germany). Galectin-3 positive areas were analyzed by ImageJ software (https://fiji.sc/) applying a manual threshold. Results are expressed as a percentage of Galectin-3 positive areas/total area of the ROI.

2.5.3. Evaluation of cardiomyocyte cross sectional area

For the evaluation of the cardiomyocyte cross sectional area (CSA), sections were stained by anti-Laminin antibody and were imaged on an ImageXpress Confocal MC system (Molecular Devices, CA, USA) with a PlanApoLambda 20×/0.75 for two channels: DAPI (nuclei), Alexa 488 (Laminin). A grid with multiple images was collected, to cover each entire section. Image analysis and object segmentation were carried out using ArivisVision4D software (Zeiss, Germany) (Supplementary Fig. S3). Regions of interest (ROIs) corresponding to specific areas of the LV (either the free wall or septum) were manually defined (Supplementary Fig. S 2). The unstained area ("hole") within each cardiac fiber was detected using a Simple Threshold algorithm, while Laminin staining was identified using a Local Adaptive Threshold algorithm. Laminin staining was associated with the corresponding cardiac fiber only if its contour fully enclosed the fiber (Supplementary Fig. S3). The two objects —"hole" and contour— were combined to form the "cardiac fiber object". The areas of individual cardiac fiber objects were then exported for statistical analysis. Notably, to ensure comparability across samples, all were segmented with the same parameters. Total cardiac fiber measurements were filtered to exclude longitudinal structures, retaining only cells presenting roundness >0.5 and long-to-short-side ratio <3. Mixed effects models were fitted separately for each combination of day (7 or 28) and tissue type (free wall or septum), using R packages *lmerTest* and *emmeans*. The nested structure of sampling sites within heart samples was appropriately handled by including random effects for sampling sites and samples (formula: $area \sim genotype + (1|sample:site)$). Estimated marginal means, with 95 % confidence intervals, were used to graphically depict differences between genotypes.

2.5.4. Identification of myofibroblasts

For identifying myofibroblasts, sections were stained by α-SMA and were imaged on an ImageXpress Confocal MC system (Molecular Devices, San Jose, CA, USA) with a PlanApoLambda 20×/0.75 for two channels: DAPI (nuclei), 488 (α-SMA). A grid with multiple images was collected, to cover the entire section. Image analysis and object segmentation were performed using ImageJ software (https://fiji.sc/).

The tissue size within each ROI (septum and free wall) was determined using low threshold setting on the DAPI channel, while areas of α-SMA positive staining were identified on channel 488 using a manual threshold. The sum of the α-SMA object's areas and tissue area were exported for statistical analyses. Consistent segmentation parameters were applied to all samples to ensure comparable results. Results are expressed as a percentage of α-SMA positive areas/total area of the ROI. For the quantification of the arterial density in the entire LV, the α-SMA positive arterioles and arteries, with a minimum internal diameter ranging from 4 μm to 170 μm, were identified on the channel 488 and quantified manually using the software ArivisVision4D (Zeiss, Germany). The number of the α-SMA objects and the tissue area were exported for statistical analyses. Results were expressed as the number of total α-SMA positive arteries/total area of the LV.

2.5.5. Evaluation of cardiac fibrosis

Collagen fibers were stained by Sirius Red staining (Direct Red 80, Sigma #365548, Merck, Germany) using a standard protocol [25]. Images of the whole section of the hearts were acquired by Aperio AT2 digital scanner at magnification of 200× (Leica Biosystems, Germany). The Sirius Red positive areas were analyzed by ImageJ software (https://fiji.sc/) applying a manual threshold. Results are expressed as a percentage of Sirius Red positive areas/total area of the ROI.

2.6. In vitro experiments

2.6.1. Isolation of cardiac fibroblasts

Cardiac fibroblasts (CFs) were isolated as previously described [33]. Before the isolation, Wt and Tg-210 mice were fed with food pellets containing doxycycline 2000 mg/kg (Mucedola, Italy) ad libitum for 10 days. Briefly, mouse hearts were perfused, the ventricles were collected and washed to remove residual red blood cells. The hearts were minced and placed in a digestion solution containing 2 mg/mL collagenase type IV (#LS004188, Worthington, USA), 1.2 U/mL Dispase I (#D4693, Merck, Sigma Aldrich, Germany), and 20 U/mL DNase I (#DN25 Merck, Sigma Aldrich, Germany). The cell suspension obtained after three rounds of 20-min digestions was passed through a 40-μm cell strainer and kept on ice throughout the procedure. Finally, CFs were plated in a 6-well plate (one heart per well) pre-coated with a 0.1 % gelatin solution (w/v) (#ES-006 EmbryoMax, Merck Life Science, Germany) and cultured in Dulbecco's Modified Eagle Medium (DMEM; #D6546, Merck, Sigma Aldrich, Germany) supplemented with 10 % fetal bovine

serum (FBS, #A5670801, Gibco, Thermo Fisher Scientific, MA, USA), 100 U/mL penicillin, and 100 μg/mL streptomycin (#ECB3001D, Euroclone, Italy) and 1 ng/mL doxycycline (#D5207, Sigma Aldrich, Germany). After 3 h of incubation, non-adherent cells were removed by replacing the culture medium, while attached cells (mainly fibroblasts) were washed and cultured in fresh media until confluent. These cells were considered as passage 0 (P0) and subsequently passaged for up to two additional times (P1–P2) for their use in functional experiments.

2.6.2. Proliferation assay

The Cell Counting Kit-8 (CCK-8) (#96992 Merck, Sigma Aldrich, Germany) was used to evaluate the proliferation of CFs. In brief, 2×10^3 cells/well were seeded into a 96-well plate pre-coated with 0.1 % gelatin solution (w/v) (#ES-006, EmbryoMax, Merck Life Science, Germany) and incubated with 1 ng/mL doxycycline (#D5207, Sigma Aldrich, Germany) for 24, 48, 72 and 96 h. Next, according to the manufacturer's protocol, 10 μL of CCK-8 solution was added to the culture medium in each well, and the plates were incubated for 4 h at 37 °C. Absorbance at 450 nm was measured using a microplate reader (Varioskan Lux, Thermo Fisher Scientific, MA, USA).

2.6.3. Cell adhesion assay

CFs were seeded into 48-well plates coated with 0.1 % gelatin solution (w/v) (#ES-006, EmbryoMax, Merck Life Science, Germany) at a concentration of 2×10^4 cells per well and incubated with 1 ng/mL doxycycline (#D5207, Sigma Aldrich, Germany). After incubation at 37 °C in 5 % CO_2 for 2, 4, and 6 h, the medium was aspirated, and cells were washed twice with PBS to remove non-adherent cells. Adherent cells were fixed with 4 % paraformaldehyde (PFA, #SC281692, Chem Cruz, Santa Cruz biotechnology, CA, USA) and stained with Hoechst 33342 (#62249, Thermo Fisher Scientific, MA, USA) at a concentration of 5 μg/mL. The attached and stained cells were quantified by measuring the fluorescence (Ex 346 nm, Em 460 nm) using a microplate reader (Varioskan Lux, Thermo Fisher Scientific, MA, USA).

2.6.4. Scratch Wound assay

CF migration was assessed using the IncuCyte Scratch Wound 96-Well Real-Time Cell Migration and Invasion Assay (Sartorius, Germany). Cells were seeded at a density of 2×10^4 cells per well in growth medium containing 0.5 % fetal bovine serum (FBS) and 1 ng/mL doxycycline (#D5207, Sigma Aldrich, Germany) in IncuCyte ImageLock 96-well plates (Sartorius, Germany) pre-coated with 0.1 % (w/v) gelatin to ensure proper attachment. The cells were allowed to form a confluent monolayer over 24 h under serum-starved conditions. Monolayers were then scratched using the IncuCyte 96-Well WoundMaker tool (Sartorius, Germany) to create consistent, wide wound areas. Wells were washed with growth medium to remove cell debris and cultured with fresh medium containing 1 ng/mL doxycycline (#D5207, Sigma Aldrich, Germany). The plates were placed in the IncuCyte Live Cell Analysis System (Sartorius, Germany). Measurements were performed automatically every 2 h for 40 h. Wound density, defined as the ratio of cell density within the wound area to the cell density outside the wound, was calculated in real-time using the system's built-in analysis algorithms. Mixed effects models were employed using R package *lmerTest*, to assess difference in the rate of wound density change over time between the two genotypes. The interaction between genotype and time was modeled as a fixed effects variable, using the sample ID as a random effects variable to account for variability between subjects (formula: $density \sim genotype*time + (1|sample)$). To assess differences between groups in each time point, the same model was re-fitted using time as a factor and R package *emmeans* was used to perform estimated marginal means *post-hoc* testing at a Benjamini-Hochberg (BH) adjusted p-value threshold of 0.05.

2.6.5. Chemotaxis cell migration assay

CF chemotaxis was evaluated using the Incucyte Chemotaxis Cell Migration Assay Clearview system (Sartorius, Germany). Both the insert side and reservoir side of the wells were pre-coated with 0.1 % (w/v) gelatin (#ES-006 EmbryoMax, Merck Life Science, Germany). CFs were seeded at 1×10^3 cells/well into the IncuCyte Clearview 96 well insert in growth medium containing 0.5 % FBS and 1 ng/mL doxycycline. A chemoattractant (200 μL of 10 % FBS) (FBS; #A5670801, Gibco, Thermo Fisher Scientific, MA, USA) or control (200 μL of PBS) was added to the reservoir plate. The plates were equilibrated at 37 °C and imaged using the IncuCyte Live-Cell Analysis System (Sartorius, Germany) every 1 h for 24 h with a 4× objective under phase contrast to assess cell motility. Mixed effects models (lmerTest) were fitted separately for samples treated with chemoattractant (FBS) and untreated samples, assessing difference in the rate of migration over time between the two genotypes. The interaction between genotype and time was modeled as a fixed effects variable, using the sample ID as a random effects variable to account for variability between subjects (formula: $area \sim genotype*time + (1|sample)$). R package emmeans was used to perform estimated marginal means *post-hoc* testing at a BH adjusted p-value threshold of 0.05, after re-fitting the models using time as a factor.

2.7. Statistical analysis

As opportune, variables were analyzed by Student's t, Mann Whitney and ANOVA tests. All tests were performed 2-sided and a $p < 0.05$ was considered as statistically significant. Continuous variables were expressed in column scatter graphs, showing mean and standard deviation. GraphPad Prism v.4.03 software (GraphPad Software Inc.) was used for statistical analysis.

3. Results

3.1. miR-210 overexpression induces eccentric hypertrophy upon TAC

To investigate miR-210 role in pressure overload-induced cardiac remodeling, we used a doxycycline-inducible miR-210 transgenic mouse strain (Tg-210) that we had generated and validated in the past [29]. miR-210 overexpression was induced by doxycycline administration starting 7 days before TAC and cardiac remodeling was assayed 7 and 28 days after surgery (Supplementary Fig. S1). Doxycycline was also administered to control Wt mice to account for potential side effects of the drug.

Cardiac remodeling following TAC was first investigated by echocardiography in both Tg-210 and Wt mice. The measure of the peak gradient, carried out on the aortic arch at the constriction site, indicated that gradients of similar intensities were induced in Wt and Tg-210 TAC mice (Supplementary Fig. S4). The m-mode analysis of cardiac function showed that fractional shortening (FS%) was significantly decreased in both Wt and Tg-210 TAC mice compared to Sham mice at 7 days (Fig. 1 A) and remained low at day 28 (Fig. 1 I), indicating decreased cardiac contractility after TAC. The left ventricular mass (LV mass) was significantly increased in both Wt and Tg-210 TAC mice compared to Sham at 7 and 28 days after TAC (Fig. 1 B and L), indicating cardiac hypertrophy. The left ventricular volume (LV Vol) at day 7 increased only in systole in both the TAC groups compared to Sham (Fig. 1C, D). Interestingly, the LV Vol was significantly increased in Tg-210 TAC mice compared to both Sham and Wt TAC mice in both diastole and in systole at day 28 (Fig. 1 M, N), indicating that cardiac remodeling leads to LV dilatation in Tg-210 mice only. The left ventricular internal diameter was increased accordingly (Fig. 1 E, F, O, and P). Finally, the left ventricular posterior wall (LVPW) showed an increase only in diastole at day 7 in Wt and Tg-210 TAC mice compared to Sham (Fig. 1 G, H). At day 28, LVPW remained high only in Wt mice in diastole and systole compared to Tg-210 TAC mice (Fig. 1 Q, R), again in keeping with LV dilatation inTg-210 mice only. Taken together, these results highlight that Wt mice developed concentric hypertrophy after TAC, while Tg-210 mice developed more severe eccentric hypertrophy.

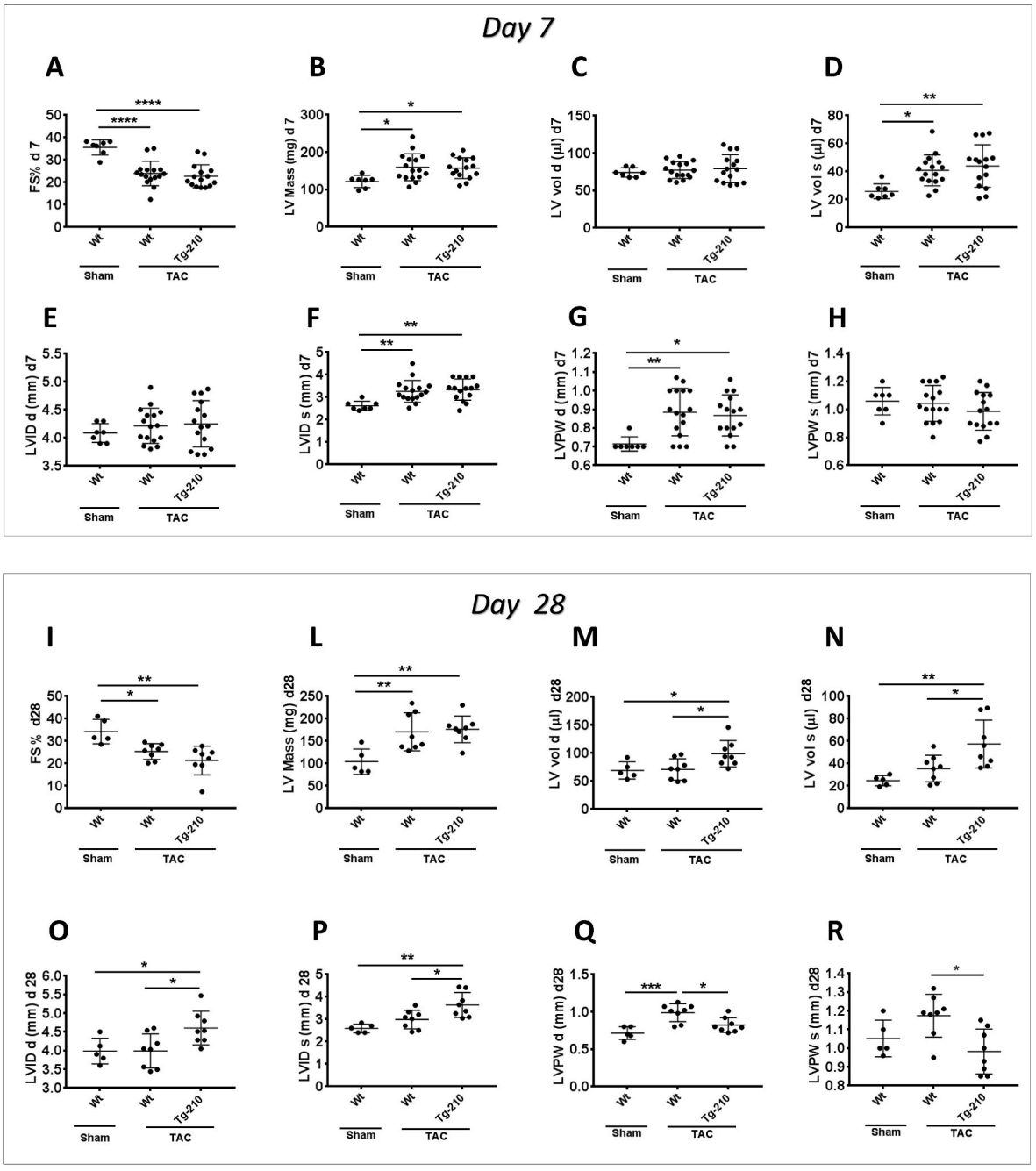

Fig. 1. Tg-210 TAC mice develop eccentric hypertrophy. Wt and Tg-210 mice were treated with doxycycline starting from 7 days before TAC surgery and until the endpoint of the experiment. All the Wt and Tg-210 TAC mice underwent echocardiography at day 7 after surgery and then were randomly assigned to two different groups. The first one was sacrificed at day 7. The second one was analyzed and sacrificed at day 28. (A–H) M mode echocardiographic results at day 7. (I–R) M mode echocardiographic results at day 28. (A and I) The percentage of fractional shortening (FS%) *P < 0.02, **P < 0.001, ****P < 0.0001; (B and L) the left ventricular mass (LV mass) *P < 0.04, **P < 0.009; (C and M) the left ventricular volume in diastole (LV vol d) *P < 0.05; (D and N) the left ventricular volume in systole (LV vol s) *P < 0.03 **P < 0.007; (E and O) the left ventricular internal diameter in diastole (LVID d) *P < 0.03; (F and P) the left ventricular internal diameter in systole (LVID s) *P < 0.02, **P < 0.002; (G and Q) the left ventricular posterior wall in diastole (LVPW d) *P < 0.01, **P < 0.004, ***P < 0.0007; (H and R) the left ventricular posterior wall in systole (LVPW s) **P < 0.009. Anova multiple comparison.

Echocardiography data did not indicate a difference in LV mass between Wt and Tg-210 TAC mice. However, to assess whether a difference was present also under this aspect, we investigated the expression of early and sensitive markers of hypertrophy, Natriuretic peptide A (Nppa) and B (Nppb) [34], in the LV (Fig. 2). Increased Nppa levels were observed in Tg-210 mice compared to Wt already at day 7 after TAC (Fig. 2 A), while both Nppa and Nppb showed significantly higher expression levels in Tg-210 mice compared to Wt at day 28 after surgery (Fig. 2C and D).

To investigate this aspect also at cellular level, the cross-sectional area (CSA) of the cardiomyocytes was measured on Laminin-stained transversal sections of TAC LVs (Supplementary Fig. S3), at 7 and 28 days after surgery. Specifically, to evaluate the CSA more accurately, the LV was divided into two ROI (Supplementary Fig. S2): the septum and the free wall [35,36]. High resolution images were obtained and the cardiomyocyte CSA was assessed algorithmically and exported for analysis, employing mixed effects linear modelling to model cell area using genotype as a fixed effect, and sites within samples as nested

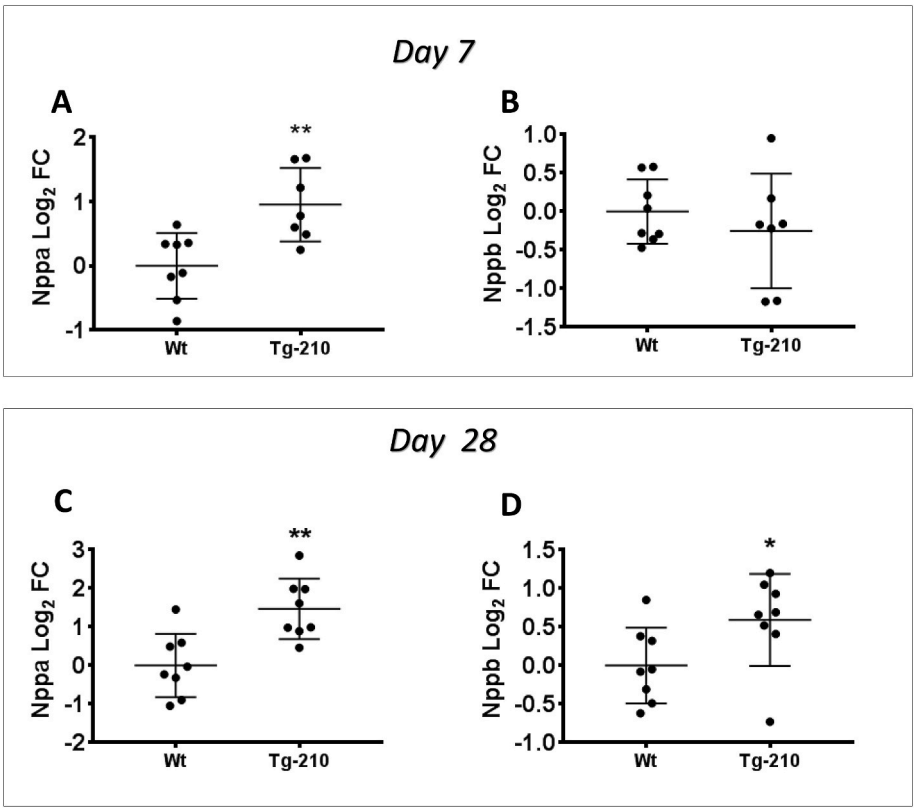

Fig. 2. LV of Tg-210 TAC mice showed increased expression levels of hypertrophy markers. RNA was extracted from left ventricles of Wt and Tg-210 TAC mice and the expression levels of hypertrophy markers were measured by qRT-PCR at day 7 (A–B) or 28 post surgery (C–D). (A and C) Natriuretic peptide A (Nppa); (B and D) Natriuretic peptide B (Nppb). Scatter plots represent mean ± SD. Values are expressed using a $\log_2$ scale (-ΔΔCt). Test t *P < 0.05, **P < 0.009.

random effects (Supplementary Fig. S5). CSA was significantly increased in the free wall of Tg-210 TAC mice at day 28 (Suppl. Fig. S5 C), in keeping with the expression levels of Nppa and Nppb (Fig. 2 C and D). At day 7, CSA increase in the free wall exhibited only a borderline significance (P = 0.08) (Supplementary Fig. S5 A). The findings are suggestive of a modest asymmetric hypertrophic effect induced by miR-210,

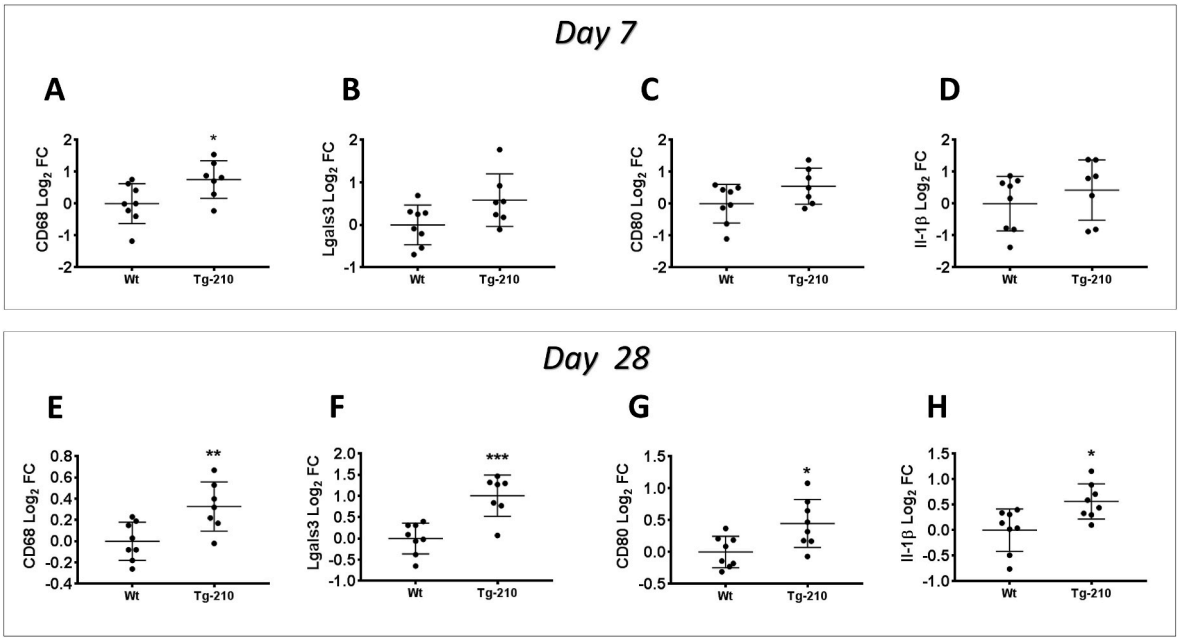

Fig. 3. LV of Tg-210 TAC mice showed increased expression levels of macrophages markers. RNA was extracted from left ventricles of Wt and Tg-210 TAC mice and the expression levels of macrophages markers were measured by qRT-PCR at 7 (A–D) or 28 days from surgery (E–H). (A and E) CD68; (B and F) Galectin-3 (Lgals3); (C and G) CD80; (D–H) Interleukin-1beta (Il-1β). Scatter plots represent mean ± SD. Values are expressed using a $\log_2$ scale (-ΔΔCt). Test t *P < 0.05, **P < 0.009, ***P < 0.0005.

impacting the free wall and sparing the septum.

3.2. Increased inflammation in the LV of Tg-210 TAC mice

Given the pivotal role of macrophages in cardiac remodeling after pressure overload [8,9] and miR-210 role in the regulation of macrophage function [24,25], the expression levels of macrophage markers were measured in LVs of TAC mice, at 7 and 28 days after surgery. Specifically, the markers measured included CD68, a pan-macrophage marker [37], Galectin-3, a marker of activated macrophages [38], CD80, which is expressed by different types of inflammatory cells including M1 macrophages, dendritic cells, and activated B-cells [37] and Interleukin-1β (Il-1β), a macrophage-derived proinflammatory cytokine [37]. Fig. 3 shows that CD68 was increased already at day 7 (Fig. 3 A) and that at day 28, all the measured markers were increased in Tg-210 TAC mice compared to Wt (Fig. 3 E–H). Together, these data indicate increased inflammation in the LV of Tg-210 mice following pressure overload.

Interestingly, the immunohistochemical staining for Galectin-3 showed that Galectin-3 was expressed not only by macrophages but also by other myocardial cell types, as previously reported (Supplementary Fig. S6 A) [39]. Given the pro-fibrotic role of Galectin-3 [40,41], the positive areas for this staining were quantified in the septum and in the free wall (Supplementary Figs. S2 and S6 B) [35,36]. Interestingly, the percentage of Galectin-3 positive areas (Supplementary Fig. S6 C-F) was significantly increased in the septum of Tg-210 TAC LV compared to Wt at day 7 (Supplementary Fig. S6 C), while no significant differences were observed at day 28.

3.3. Fibrosis is increased in the LV of Tg-210 mice upon TAC

Fibrosis is a hallmark of LV remodeling upon pressure overload [42]. To clarify the distribution of the collagen in the heart, transversal sections of TAC LV were stained by Sirius red (Fig. 4 A–B and E–F) and the percentage of Sirius red positive areas was evaluated. Also in this case, the septum and the free wall were analyzed separately (Supplementary Fig. S2). At day 7, Sirius red-positive fibers were localized mainly in the septum, displaying interstitial and perivascular fibrosis (Fig. 4 A and B). Accordingly, the percentage of the Sirius red positive areas was significantly higher in the septum of Tg-210 TAC LV compared to Wt (Fig. 4 C), while no difference was observed in the free wall (Fig. 4 D). On day 28, Sirius red staining was spread and intense in Wt and Tg-210 TAC LV, indicating collagen accumulation in interstitial and perivascular areas (Fig. 4 E and F). The quantification showed that the percentage of the Sirius red positive areas was significantly increased in the free wall of Tg-210 TAC compared to Wt TAC (Fig. 4 H), while no differences were observed in the septum (Fig. 4 G), indicating a difference in the fibrosis dynamics between Tg-210 and Wt mice upon TAC.

In order to further delineate the development of fibrosis in Tg-210 TAC mice, an analysis was undertaken to evaluate the mRNA levels of the Collagen I chains, Col1A1 and Col1A3, and of Myosin heavy chain 10 (Myh10), a conventional non-muscle myosin involved with LARP6 in the stabilization of type I collagen mRNAs. Col1A1 and Myh10 were more expressed in Tg-210 TAC LV compared to Wt at day 7 (Fig. 4 I–M), while no statistically significant difference was found at day 28 (Fig. 4 N–P).

Next, the expression of Alpha smooth muscle actin 2 (Acta 2) mRNA, a marker of both myofibroblasts and arterial wall, was assessed. Acta2 was more expressed in the LV of Tg-210 TAC mice at 7 and 28 days than in Wt TAC (Fig. 5 A and B). To confirm these results, the product of the Acta2 gene, α-smooth muscle actin (α-SMA) protein was detected by immunofluorescence on transversal sections of TAC hearts (Fig. 5 C–F). To quantify the percentage of α-SMA positive areas upon TAC (Fig. 5 G–L), the septum and the free wall were assessed individually. The percentage of α-SMA positive areas was significantly higher in the septum of Tg-210 compared to Wt mice at day 7 (Fig. 5 G) while no differences were observed in the free wall (Fig. 5 H). As previously reported, the intensity of the α-SMA staining was strongly decreased or completely missing in the myofibroblasts at day 28 [43], remaining detectable in the arterial wall (Fig. 5 E and F). Thus, Wt and Tg-210 TAC LV did not show any difference in the percentage of α-SMA positive areas at this later time point.

To clarify if the differences observed in the percentage of α-SMA positive areas at day 7 could be due, at least in part, to an angiogenic process, the arterial density was quantified in LV sections stained for α-SMA (Fig. 5 C and D). The analysis showed no differences in the arterial density between Wt and Tg-210 TAC LV at day 7 (Suppl. Fig. S7 A). Accordingly, the expression levels of the angiogenic growth factors Vefg-A, Fgf-1 and their receptors (Flt-1 and Fgfr-1, respectively) did not show any difference between Wt and Tg-210 TAC LV (Supplementary Fig. S7 C-F). Next, arterial density was assessed also at day 28, identifying a significant increase of the arterial density in Tg-210 TAC LV compared to Wt (Fig. 5 E–F and Supplementary Fig. S7 B). The expression levels of Vefg-A, Fgf-1 and their receptors were increased accordingly (Supplementary Fig. S7 G-L).

Subsequently, we evaluated the expression of two main pro-fibrotic factors: Transforming growth factor β1 (Tgf-β1), playing a pivotal role in collagen accumulation and fibrosis in several diseases [6,44], and Connective tissue growth factor (Ctgf), a pro-fibrotic factor strongly implicated in cardiac fibrosis [45,46] (Supplementary Fig. S8). The qRT-PCR analysis showed no differences in the expression levels of Tgf-β1 and Ctgf in Wt and Tg-210 TAC LV at day 7 (Supplementary Fig. S8 A-B). Interestingly Tgf-β1 and Ctgf were significantly more expressed in Tg-210 TAC LV than in Wt at day 28 (Supplementary Fig. S8 C-D).

These results show that, under pressure overload, miR-210 overexpression leads to increased interstitial and perivascular fibrosis.

3.4. miR-210 enhances cardiac fibroblast adhesion and migration in vitro

To determine whether the effects of miR-210 on cardiac fibrosis are mediated by miR-210 action on CFs, *in vitro* experiments were performed. Adult CFs from both Wt and Tg-210 healthy ventricles were isolated and cultured to assess proliferation (Supplementary Fig. S9), adhesion, wound healing and migration (Figs. 6–8). Cells were imaged daily during the first 96 h of culture (Supplementary Fig. S9 A). The over-expression of miR-210 in CFs derived from Tg-210 mice compared to those from Wt mice was confirmed (Supplementary Fig. S9 B). No consistent differences were observed in proliferation between Wt and Tg-210 CFs cultured over 96 h (Supplementary Fig. S9 C). However, a small but significant difference was observed at 24 h post-seeding, when miR-210-overexpressing CFs exhibited significantly higher values compared to Wt CFs. Thus, we hypothesized that Tg-210 CFs may exhibit enhanced adhesion to the gelatin-coated substrate. When the adhesion of CFs to the gelatin-coated substrate was assessed, it was found that Tg-210 CFs adhered more efficiently than Wt CFs (Fig. 6).

CF migration is crucial in the cardiac wound healing response, as its increase is indicative of CF activation [12]. Therefore, scratch assays were conducted to evaluate planar motility differences between Tg-210 and Wt CFs. Fig. 7 shows a statistically significant increase in the rate of wound closure in Tg-210 CFs compared to Wt. Additionally, significant differences were observed at individual time points between 6 and 26 h (Fig. 7 B). To further evaluate CFs migration, a cell chemotaxis assay was performed. Using FBS as a chemoattractant, Tg-210 CFs exhibited a significantly higher migration rate over time compared to Wt CFs (Fig. 8).

Taken together these results demonstrate that CFs over-expressing miR-210 show increased capacity of adhesion, wound healing and migration toward FBS. These peculiar features of CFs over-expressing miR-210 may contribute to explain the increased cardiac fibrosis observed in Tg-210 TAC LVs.

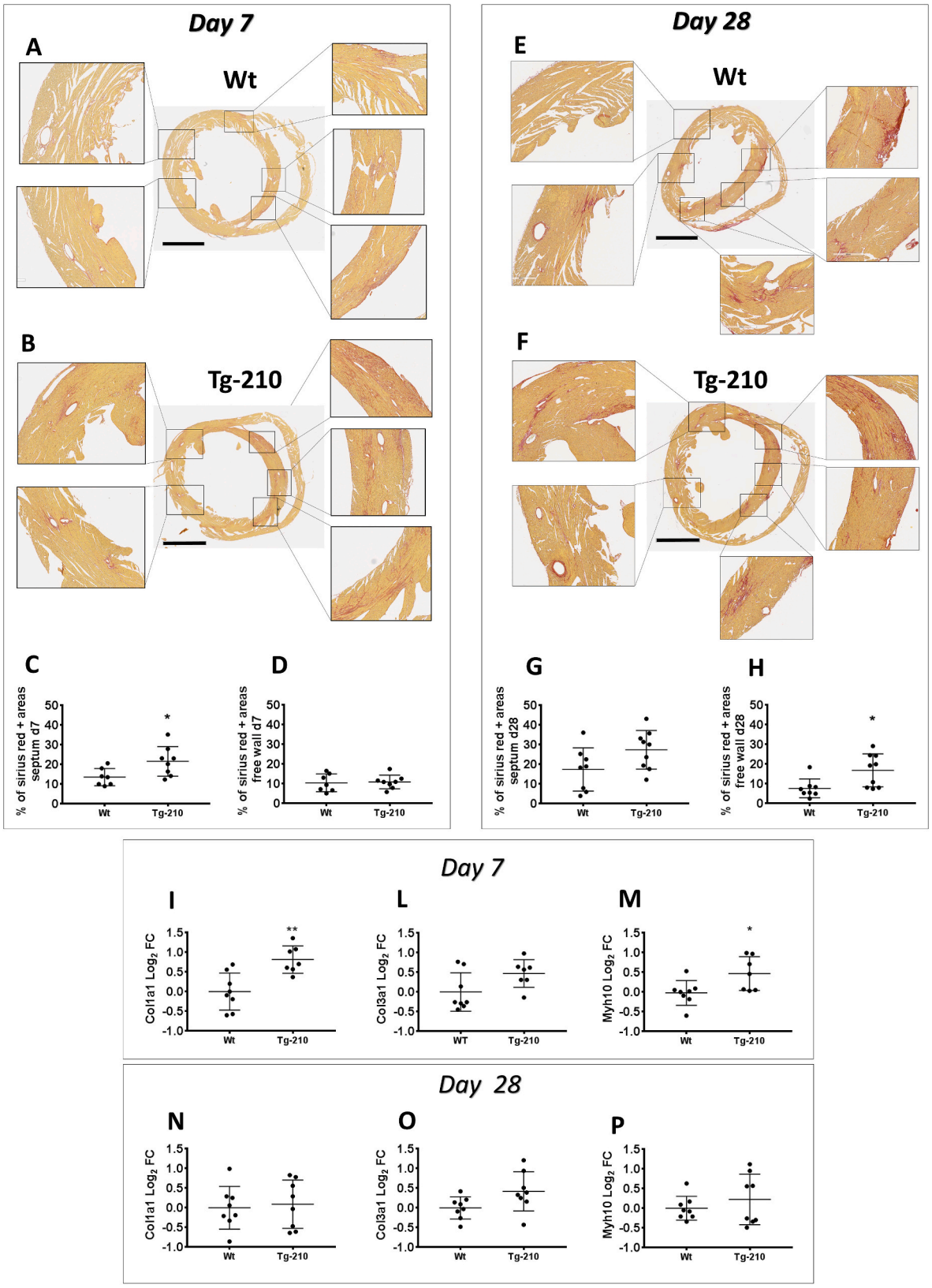

Fig. 4. miR-210 overexpression increased tissue fibrosis after pressure overload. (A–B and E-F) Representative Sirius red staining of Wt and Tg-210 TAC LVs at day 7 (A–B) and 28 (E–F). Calibration bar 2 mm. Quantification of the percentage of Sirius red positive areas in the septum (C and G) and in the free wall (D and H) at 7 (C and D) and 28 days (G and H). Scatter plots represent mean ± SD. Mann Whitney test *P < 0.03. (I–P) RNA was extracted from LVs of Wt and Tg-210 TAC mice and the expression levels of fibrosis markers were measured by qRT-PCR at 7 (I–M) and 28 days (N–P) after surgery. (I and N) expression levels of Col1A1; (L and O) expression levels of Col3a1; (M and P) expression levels of Myh10. Scatter plots represent mean ± SD. Values are expressed using a $\log_2$ scale (-ΔΔCt). Test t *P < 0.02, **P < 0.002.

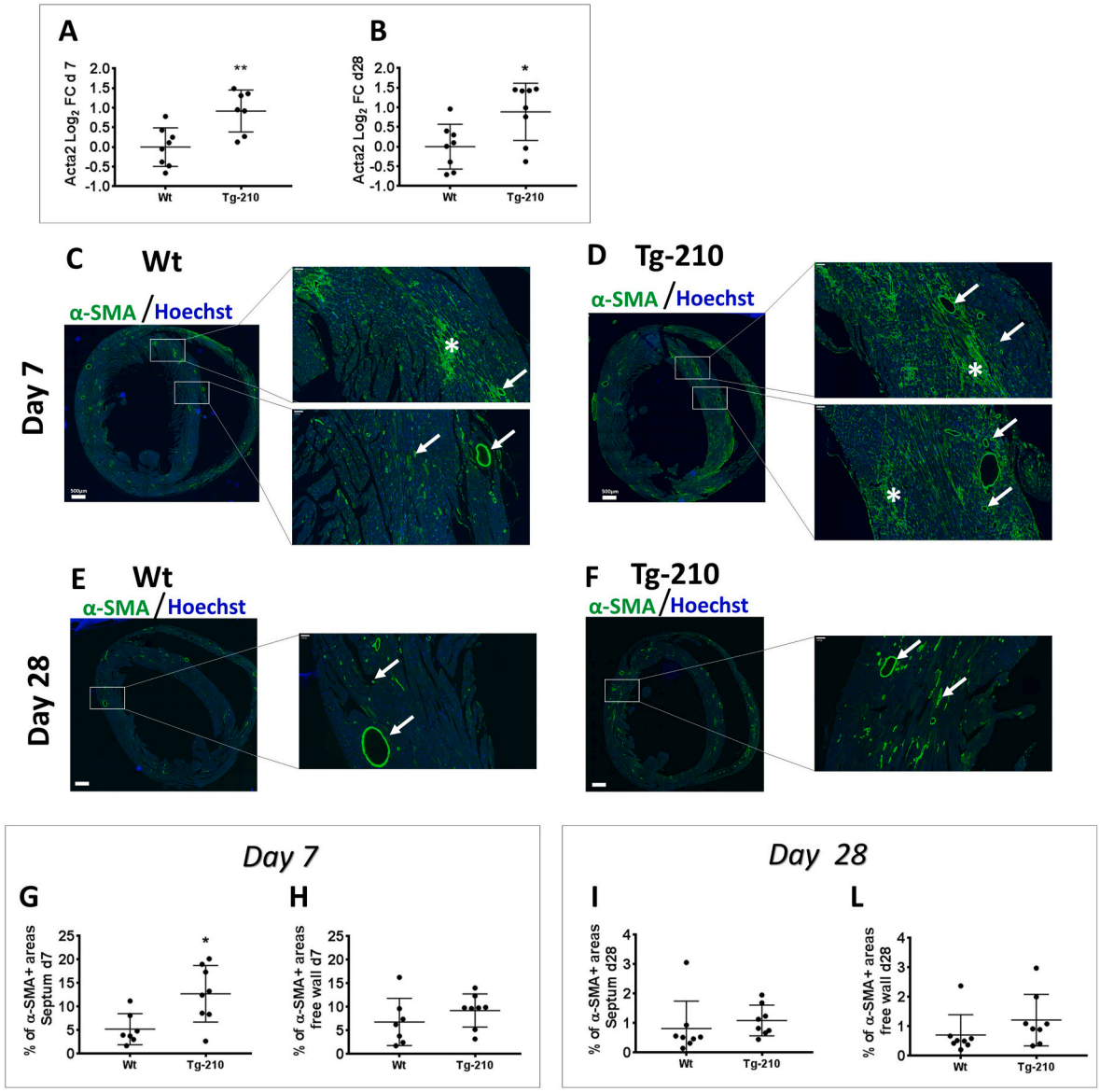

Fig. 5. Characterization of α-SMA expression in Wt and Tg-210 TAC LVs at day 7 and 28. (A–B) RNA was extracted from LVs of Wt and Tg-210 TAC mice and the expression level of the myofibroblast marker actin alpha 2, smoot muscle (Acta2) was measured by qRT-PCR at day 7 and 28 post surgery. Scatter plots represent mean ± SD. Values are expressed using a $\log_2$ scale (-ΔΔCt). Test t *P < 0.02, **P < 0.005. (C–F) Representative immunofluorescence staining for alpha-smooth muscle actin (α-SMA) of Wt and Tg-210 TAC LVs. α-SMA positive cells were stained in green. Nuclei were stained by Hoechst (Blue). α-SMA stains both myofibroblasts and smooth muscle cells in the tunica media of the arteries. The insets show the enlargement of selected regions. White arrows indicate arteries, white asterisks indicate myofibroblasts. Calibration bar 500 μm. (G–L) Quantification of the percentage of the α-SMA positive areas in the septum (G and I) or in the free wall (H and L) of Wt and Tg-210 TAC mice. (G–H) Quantification at day 7. (I–L) Quantification at day 28. Scatter plots represent mean ± SD. Test t *P < 0.01.

3.5. HIF pathway activation in LV of Tg-210 TAC mice

It has been shown that a hypoxia-induced positive feedback loop promotes HIF-1a stability through miR-210 [47,48] and that chronic cardiac HIF-1a stabilization is deleterious for the heart [49–51]. Interestingly, Vefg-A is a direct transcriptional target of HIF-1 and it was found to be significantly more expressed in the Tg-210 TAC LV than in Wt (Supplementary Fig. S7 G). Therefore, in order to investigate if the HIF pathway is constitutively activated in the LV of Tg-210 TAC mice, the mRNA level of other HIF-1 responsive genes was measured at 7 and 28 days (Fig. 9). The expression of HIF-1 target genes involved in glycolysis, including phosphoglycerate kinase 1 (Pgk1), solute carrier family two member 1 (Slc2a1 or Glut-1) and alpha-enolase (Eno1) was significantly increased in the LV of Tg-210 TAC mice compared to Wt at day 28 (Fig. 9 A, B, C). Likewise, the level of the peroxisome proliferator-activated receptor gamma (Ppar-γ), a key mediator in lipid anabolism, and a direct transcriptional target of HIF-1 in cardiomyocytes [52], as well as the level of the apoptosis modulator Bcl2 Interacting Protein 3 (Bnip3) [51] were also significantly upregulated at day 28 (Fig. 9 D and E).

These results suggest that, one possible mechanism by which the constitutive expression of miR-210 may promote adverse cardiac remodeling involves the activation of a positive feedback loop that promote HIF-1α stability.

4. Discussion

In this study, we investigated the role played by miR-210 in cardiac remodeling and fibrosis induced by pressure overload.

The echocardiography results at 28 days after TAC showed that, in

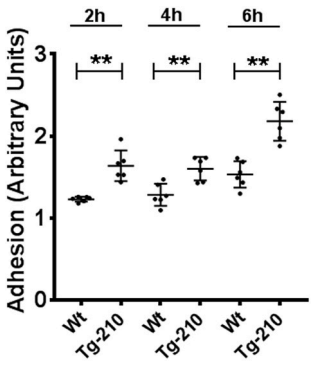

Fig. 6. miR-210 overexpression enhance CFs adhesion. CFs were seeded on gelatin coated support and adhesion was measured at the indicated times; after fixation, the cells were stained by Hoechst 33342 and quantified by fluorescence measurement. miR-210 over-expressing Tg-210 CFs show increased adhesion compared to Wt CFs. Data are presented as scatter plots showing the mean ± SD (n = 6; **P < 0.01).

Wt TAC mice, pressure overload induces concentric hypertrophy, since they showed increased LV mass and LV posterior wall thickness and reduced FS% compared to Sham-operated mice. However, the over-expression of miR-210 in Tg-210 TAC mice induces eccentric hypertrophy, since these mice showed not only decreased FS% and increased LV mass compared to Sham-operated mice, but also increased chamber volume and diameter [53]. In the analysis of different cardiac remodeling markers, Tg-210 TAC LV showed increased expression levels of hypertrophy markers Nppa and Nppb. This finding was further corroborated by the quantification of the CSA of cardiomyocytes, indicating a modest asymmetric hypertrophic effect of miR-210, impacting the free wall, that was not evident by echocardiography.

Concentric hypertrophy can lead to moderate systolic dysfunction. In contrast, eccentric hypertrophy leads to a more severe dysfunction, characterized by myocardial stiffness due to interstitial fibrosis and both diastolic and systolic dysfunctions [53]. Therefore, echocardiographic and hypertrophy–marker data indicate that mice over-expressing miR-210 develop more severe cardiac disease than Wt.

The analysis of the expression levels of macrophage markers showed that, in Tg-210 TAC LV, the inflammation persisted until day 28 and it was higher than in Wt TAC. These results suggest a role of miR-210 in the modulation of the inflammatory response after pressure overload, in keeping with previous observations in different pathological contexts [24–27]. The induction of Galectin-3 in Tg-210 TAC LV was particularly interesting, as this gene is involved in inflammation and fibrosis. Indeed, while Galectin-3 was previously considered a specific marker of macrophages [54,55], more recent evidence shows that it can be expressed by other cell types, including cardiac fibroblasts [40]. Specifically,

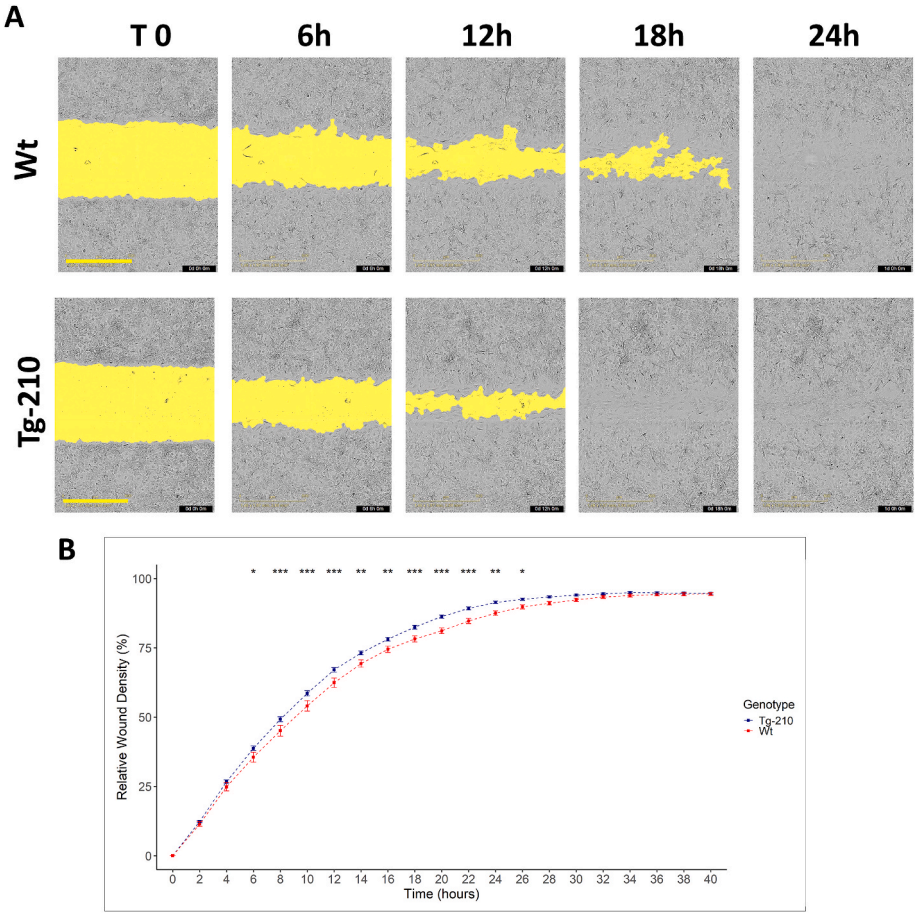

Fig. 7. Enhanced wound healing properties of Tg-210 CFs. Wt and Tg-210 CFs were seeded (2×10^4 cells per incucyte imagelock plate 96 well) and allowed to form a confluent monolayer over 24 h. Reproducible wounds were created and phase-contrast images were acquired every 2 h for 40 h. (A) Time-lapse phase images show migration of Wt and Tg-210 CFs over 24 h, with segmentation masks showing initial scratch (yellow) and wound closure over time. (B) Relative wound density (expressed in %) was automatically measured in 2-h intervals for a 40-h time span following the initiation of the scratch assay. A mixed-effects model, incorporating cross-replicate variability as a random effects variable, was used to compare wound healing rates over time between Tg-210 (N = 36) and Wt (N = 35) CFs (P = 0.039). *Post-hoc* tests were performed to assess differences at individual time points. Blue and red lines and squares correspond to Tg-210 and Wt CFs respectively. Error-bars represent Standard Error of the Mean (SEM). Estimated marginal means *post-hoc* tests, *P < 0.05, **P < 0.01, ***P < 0.001.

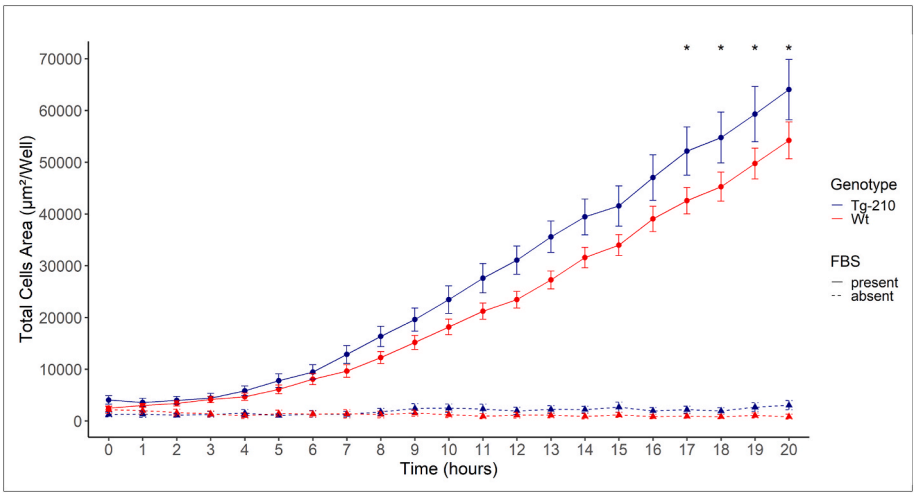

Fig. 8. The migratory capacity of Tg-210 CFs is increased compared to Wt. To test chemotaxis, 1×10^3 CFs (N = 36) were seeded into the IncuCyte Clearview 96 well insert in growth medium containing 0.5 % FBS and 1 ng/mL doxycycline. A chemoattractant (10 % FBS medium) or control (PBS) was added to the reservoir plate. The plates were equilibrated at 37 °C and imaged every hour for 20 h with a 10× objective under phase contrast to assess cell motility and migration (total cells area, μm^2/well) was assessed making automated measurements. Mixed effects models were fitted, incorporating cross-replicate variability as a random effect, to compare migration rates over time between Tg-210 and Wt CFs in the presence ($P = 3.6 \times 10^{-10}$) or absence ($P = 2 \times 10^{-16}$) of FBS. *Post-hoc* testing enabled evaluation of differences at individual time points. Blue and red lines correspond to Tg-210 and Wt genotypes respectively, while solid and dashed lines correspond to FBS presence and absence respectively. Error-bars represent Standard Error of the Mean (SEM). Estimated marginal means *post-hoc* tests, *P < 0.05.

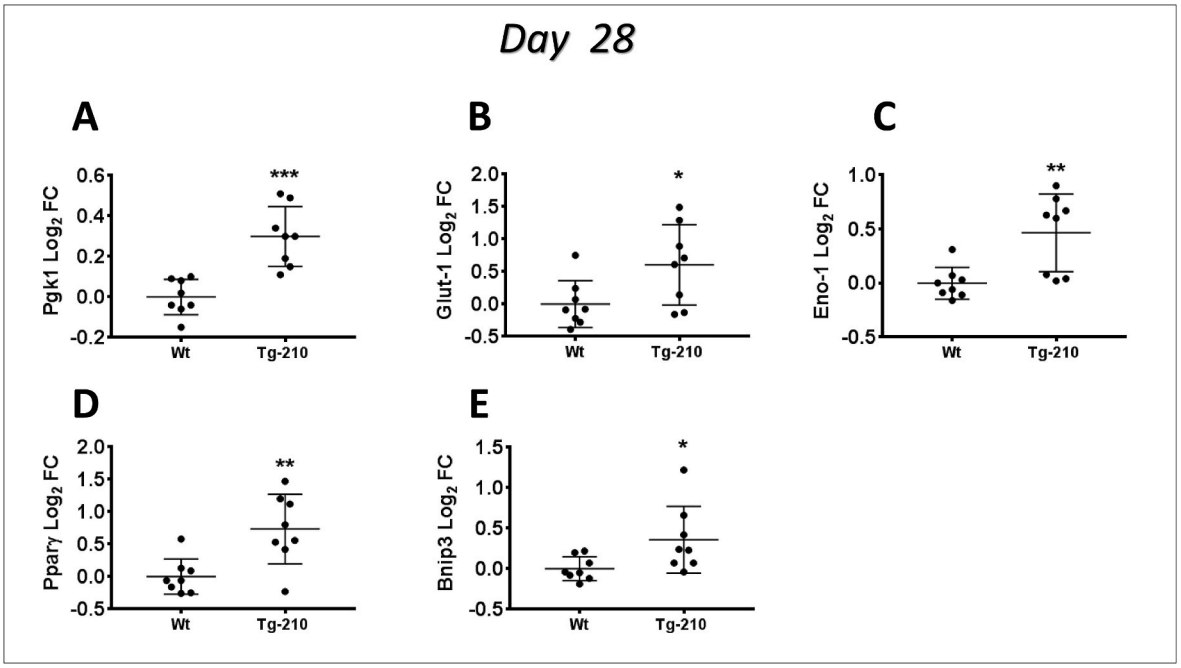

Fig. 9. HIF pathway activation in LV of Tg-210 TAC mice. (A–E) RNA was extracted from LVs of Wt and Tg-210 TAC mice and the expression levels of the HIF-1 responsive genes Pgk1 (A), Glut-1 (B), Eno1 (C), Ppar-γ (D) and Bnip3 (E) were measured by qRT-PCR at day 28 after TAC. Scatter plots represent mean ± SD. Values are expressed using a $\log_2$ scale (-ΔΔCt). Test t *P < 0.04, **P < 0.005.

Frunza and collaborators showed an early upregulation of Galectin-3 in subpopulations of macrophages and myofibroblasts, followed by a cytoplasmic immunoreactivity for Galectin-3 in a subset of cardiomyocytes, localized in the fibrotic areas [39]. Moreover, genetic disruption and pharmacological inhibition of Galectin-3 attenuates cardiac fibrosis, LV dysfunction, and subsequent heart failure development in a mouse model of cardiac remodeling obtained by angiotensin II infusion or TAC [56]. Accordingly, immunohistochemistry for Galectin-3 carried out on days 7 and 28, showed that the staining was localized in macrophages and other cell types, confirming a broader expression of Galectin-3 in our model of cardiac remodeling. Interestingly, the percentage of Galectin-3 positive areas was significantly increased in the septum of Tg-210 TAC LVs at day 7, in keeping with the quantification of the fibrotic and α-SMA positive areas. The observed discrepancy between the Galectin-3 expression levels and the percentage of Galectin-3 positive areas in LVs sections at day 7 and 28 may be due to post transcriptional regulatory mechanisms.

The analysis of collagen fibers deposition revealed interstitial and perivascular fibrosis, with an increased percentage of Sirius red-positive areas in the septum of Tg-210 TAC mice at day 7 and in the free wall at

day 28. Accordingly, the mRNA expression levels of collagens, Myh10 and pro-fibrotic growth factors Tgf-β1 and Ctgf were significantly increased. Overall, these results indicate that miR-210 overexpression after pressure overload increases tissue fibrosis.

In keeping with this interpretation, the expression of the myofibroblast marker α-SMA was also significantly increased in Tg-210 TAC LVs compared to Wt, at both 7 and 28 days. The analysis of myofibroblasts localization carried out by immunofluorescence staining for α-SMA at day 7, showed that positive cells were present in the entire LV of TAC mice. The localization of the staining indicated the presence of interstitial and perivascular myofibroblasts with an increased percentage of α-SMA positive areas in the septum of Tg-210 TAC LV compared to Wt TAC. As expected, α-SMA staining also identified the smooth muscle cells of the *tunica media* of the arteries. The analysis of the arterial density carried out in the septum and the free wall showed no differences between Wt and Tg-210 TAC LVs. Accordingly, no differences were observed in angiogenic growth factors Vegf-A and Fgf-1 expression levels and their receptors at day 7. These results highlight that the observed difference in the percentage of α-SMA positive areas was due to increased myofibroblasts and not to an angiogenic response. However, we found no difference in the percentage of α-SMA positive areas at day 28. Indeed, according to the literature, during the maturation phase, myofibroblasts disassemble their α-SMA-containing stress fibers while they continue to secrete matricellular proteins [12,43]. Interestingly, in keeping with the increased expression levels of pro-angiogenic growth factors and their receptors at day 28, an increased arterial density was observed in Tg-210 TAC LVs compared to Wt TAC, confirming a pro-angiogenic role of miR-210 also in this pathological context [57].

In vitro experiments were performed to assess how miR-210 affected CF functions. A previous study demonstrated that the upregulation of miR-210 in lung fibroblasts derived from idiopathic pulmonary fibrosis patients, promotes cell proliferation by repressing MNT, an inhibitor of c-Myc [27]. However, we did not find any difference in proliferation between Wt and Tg-210 CFs isolated from ventricles of healthy mice, possibly for organ/species differences.

On the other side, miR-210 over-expressing CFs showed increased adhesion, wound healing and migration capacity compared to Wt. These findings are in agreement with several studies, demonstrating that miR-210 enhances adhesion, migratory and proangiogenic capacities of other cell types, including endothelial cells [16,58–60] and circulating pro-angiogenic cells (PACs) [18]. miR-210-mimic transfection of human dermal fibroblasts exposed to hypoxia and high glucose decreases oxygen consumption rate, enhances glycolysis and diminishes ROS levels, leading to increased migration [61]. The miR-210-induced migration of human dermal fibroblasts exposed to high glucose levels in hypoxia is abrogated when glycolysis is inhibited, thus the enhanced glycolysis mediates the positive effects of miR-210 on migration [61]. Interestingly, we found increased expression of genes involved in glycolysis including Pgk, Glut-1 and Eno-1 in the LV of Tg-210 TAC mice compared to Wt at day 28. This is in agreement with the emerging role of glycolysis in promoting cellular processes involved in tissue repair and regeneration [62,63]. It is also been shown that intra-articular injection of miRNA miR-210 promotes the healing of partially torn anterior cruciate ligament by increasing angiogenesis and fibrotic deposition [64]. Interestingly, Kawanishi and collaborators demonstrated that intra-articular injection of synthetic miR-210 accelerates avascular healing in rat medial meniscal injured model, by promoting the collagen type 2 production from meniscus cells and by increasing VEGF and FGF2 expression in synovial cells [65]. It is tempting to speculate, that the increased adhesion/migration potential of Tg-210 CFs may be a relevant element of the pro-fibrotic response of Tg-210 mice after TAC, contributing to maladaptive cardiac remodeling.

miR-210 is a HIF-1 responsive hypoxamiR that is evolutionarily conserved and ubiquitously expressed in hypoxic cells and tissues [66,67]. During the development of cardiac hypertrophy, it has been demonstrated that a mismatch between the number of capillaries and the size of cardiomyocytes occurs, leading to myocardial hypoxia [68]. The primary factor mediating tissue response to hypoxia is HIF-1. Under hypoxic conditions, PHDs (prolyl-4-hydroxylase domain-containing enzymes) are inhibited, allowing HIF-1a stabilization, dimerization with HIF-1b and binding to the hypoxia-responsive elements of target genes that mediate hypoxia adaptive responses. While short-term upregulation of HIF-1α signaling may alleviate heart failure, different reports suggest that prolonged upregulation of HIF-1a is detrimental to the heart [49–51]. Indeed, increasing evidence shows that chronic hypoxia is actively involved in the pathogenesis of fibrosis [69]. Minamishima and collaborators demonstrated that inactivation of PHD2 leads to the development of dilated cardiomyopathy and premature mortality [50]. In addition, long-term cardiac-specific inactivation of PHD2 in mice that underwent TAC, leads to a more severe decompensation compared to control mice, myocardial enlargement, myocytes dropout and interstitial fibrosis [51]. The increased tissue fibrosis observed in Tg-210 TAC LVs, may be, at least in part, due to a miR-210-induced positive feedback loop promoting HIF-1a stability [47,48]. The pro-fibrotic signals could be predominant in this condition, despite the cardioprotective pro-angiogenic response. Further investigations are needed to investigate the mechanism by which miR-210 overexpression increases cardiac fibrosis.

In conclusion, our findings show that miR-210 overexpression during pressure overload increases LV interstitial and perivascular fibrosis and confirms the pro-angiogenic role of miR-210 observed in other conditions. Given the high pleiotropy of microRNAs, the miR-210 function needs to be tested in various physiopathological contexts. Before moving to translational applications, this accurate preclinical work is necessary to understand miRNA function fully.

CRediT authorship contribution statement

G. Zaccagnini: Writing – review & editing, Writing – original draft, Validation, Supervision, Methodology, Investigation, Formal analysis, Data curation, Conceptualization. **D. Baci:** Writing – review & editing, Writing – original draft, Methodology, Investigation, Formal analysis, Data curation, Conceptualization. **S. Tastsoglou:** Writing – review & editing, Writing – original draft, Validation, Methodology, Investigation, Formal analysis, Data curation, Conceptualization. **I. Cozza:** Writing – review & editing, Investigation, Formal analysis, Data curation. **A. Madè:** Writing – review & editing, Investigation, Formal analysis, Data curation. **C. Voellenkle:** Writing – review & editing, Formal analysis, Data curation, Conceptualization. **M. Nicoletti:** Writing – review & editing, Investigation. **C. Ruatti:** Writing – review & editing, Investigation, Formal analysis, Data curation. **M. Longo:** Writing – review & editing, Investigation, Formal analysis, Data curation. **L. Perani:** Writing – review & editing, Methodology, Investigation, Formal analysis, Data curation. **C. Gaetano:** Writing – review & editing, Validation. **A. Esposito:** Writing – review & editing. **F. Martelli:** Writing – review & editing, Writing – original draft, Validation, Supervision, Resources, Project administration, Methodology, Funding acquisition, Data curation, Conceptualization.

Declaration of generative AI and AI-assisted technologies in the writing process

During the preparation of this work the authors used ChatGPT 3.5 in order to increase readability. After using this tool/service, the authors reviewed and edited the content as needed and take full responsibility for the content of the publication.

Sources of funding

F.M., G.Z. and C. V. are partially supported by Ricerca Corrente funding from Italian Ministry of Health to IRCCS Policlinico San Donato (Ricerca corrente #1.10.120 and Ricerca Corrente #1.07.128). F.M. is

also supported by the Italian Ministry of Health (POS-T4 CAL.HUB.RIA T4-AN-09), and by the European Commission (Next Generation EU-NRRP M6C2 Inv. 2.1 PNRRMAD 2022-12375790; PNRR-MCNT2-2023-12377983, and EU PNRR-III-C9-2022-I8, CF 186/24.11.2022). C. G is supported by Italian Ministry of Health, Ricerca Corrente Reti, Progetto di Rete Aging "Next Generation Promising" and Italian Ministry of Health Ricerca Finalizzata RF-2019-12368521.

Declaration of competing interest

The authors declare that they have no known competing financial interests or personal relationships that could have appeared to influence the work reported in this paper.

Acknowledgments

Daniele Catalucci and Pierluigi Carullo are acknowledged for sharing the surgical procedure of transverse aortic constriction in mice. Part of this work was done with the assistance of the Advanced Microscopy Laboratory (Alembic) and of the Mouse Clinic of IRCCS Ospedale San Raffaele and Università Vita-Salute San Raffaele. Specifically, Valeria Berno, Cesare Covino and Amleto Fiocchi are acknowledge for their excellent support. Federica Cirillo, Marco Piccoli and Lorenzo Mornatti, IRCCS Policlinico San Donato, are acknowledged for their valuable support. Figures were partly generated by BioRender.com.

This paper is dedicated to the memory of Paola Fuschi, who passed away during this investigation.

Appendix A. Supplementary data

Supplementary data to this article can be found online at https://doi.org/10.1016/j.ncrna.2025.01.009.

References

[1] M. Rana, Aortic valve stenosis: diagnostic approaches and recommendations of the 2021 ESC/EACTS Guidelines for the management of valvular heart disease -A review of the literature, Cardiol Cardiovasc Med 6 (2022) 315–324, https://doi.org/10.26502/fccm.92920267.

[2] P.R. Goody, M.R. Hosen, D. Christmann, S.T. Niepmann, A. Zietzer, M. Adam, F. Bönner, S. Zimmer, G. Nickenig, F. Jansen, Aortic valve stenosis: from basic mechanisms to novel therapeutic targets, Arterioscler. Thromb. Vasc. Biol. 40 (2020) 885–900, https://doi.org/10.1161/ATVBAHA.119.313067.

[3] J. Joseph, S.Y. Naqvi, J. Giri, S. Goldberg, Aortic stenosis: pathophysiology, diagnosis, and therapy, Am. J. Med. 130 (2017) 253–263, https://doi.org/10.1016/j.amjmed.2016.10.005.

[4] N.G. Frangogiannis, Cardiac fibrosis, Cardiovasc. Res. 117 (2021) 1450–1488, https://doi.org/10.1093/cvr/cvaa324.

[5] Y. Xia, K. Lee, N. Li, D. Corbett, L. Mendoza, N.G. Frangogiannis, Characterization of the inflammatory and fibrotic response in a mouse model of cardiac pressure overload, Histochem. Cell Biol. 131 (2009) 471–481, https://doi.org/10.1007/s00418-008-0541-5.

[6] T.A. Wynn, K.M. Vannella, Macrophages in tissue repair, regeneration, and fibrosis, Immunity 44 (2016) 450–462. S1074-7613(16)30053-X [pii].

[7] N.G. Frangogiannis, Cardiac fibrosis: cell biological mechanisms, molecular pathways and therapeutic opportunities, Mol. Aspect. Med. 65 (2019) 70–99, https://doi.org/10.1016/j.mam.2018.07.001.

[8] Z. Ren, P. Yu, D. Li, Z. Li, Y. Liao, Y. Wang, B. Zhou, L. Wang, Single-cell reconstruction of progression trajectory reveals intervention principles in pathological cardiac hypertrophy, Circulation 141 (2020) 1704–1719, https://doi.org/10.1161/CIRCULATIONAHA.119.043053.

[9] D. Yang, H.-Q. Liu, F.-Y. Liu, N. Tang, Z. Guo, S.-Q. Ma, P. An, M.-Y. Wang, H.-M. Wu, Z. Yang, et al., Critical roles of macrophages in pressure overload-induced cardiac remodeling, J. Mol. Med. (Berl.) 99 (2021) 33–46, https://doi.org/10.1007/s00109-020-02002-w.

[10] A. Das, M. Sinha, S. Datta, M. Abas, S. Chaffee, C.K. Sen, S. Roy, Monocyte and macrophage plasticity in tissue repair and regeneration, Am. J. Pathol. 185 (2015) 2596–2606, https://doi.org/10.1016/j.ajpath.2015.06.001.

[11] J. Baum, H.S. Duffy, Fibroblasts and myofibroblasts: what are we talking about? J. Cardiovasc. Pharmacol. 57 (2011) 376–379, https://doi.org/10.1097/FJC.0b013e3182116e39.

[12] F.S. Younesi, A.E. Miller, T.H. Barker, F.M.V. Rossi, B. Hinz, Fibroblast and myofibroblast activation in normal tissue repair and fibrosis, Nat. Rev. Mol. Cell Biol. 25 (2024) 617–638, https://doi.org/10.1038/s41580-024-00716-0.

[13] S. Greco, C. Gaetano, F. Martelli, HypoxamiR regulation and function in ischemic cardiovascular diseases, Antioxidants Redox Signal. 21 (2014) 1202–1219, https://doi.org/10.1089/ars.2013.5403.

[14] S. Greco, P. Fasanaro, S. Castelvecchio, Y. D'Alessandra, D. Arcelli, M.D. Donato, A. Malavazos, M.C. Capogrossi, L. Menicanti, F. Martelli, MicroRNA dysregulation in diabetic ischemic heart failure patients, Diabetes 61 (2012) 1633–1641, https://doi.org/10.2337/db11-0952.

[15] S.Y. Chan, Y.Y. Zhang, C. Hemann, C.E. Mahoney, J.L. Zweier, J. Loscalzo, MicroRNA-210 controls mitochondrial metabolism during hypoxia by repressing the iron-sulfur cluster assembly proteins ISCU1/2, Cell Metabol. 10 (2009) 273–284, https://doi.org/10.1016/j.cmet.2009.08.015.

[16] P. Fasanaro, Y. D'Alessandra, V.D. Stefano, R. Melchionna, S. Romani, G. Pompilio, M.C. Capogrossi, F. Martelli, MicroRNA-210 modulates endothelial cell response to hypoxia and inhibits the receptor tyrosine kinase ligand ephrin-A3, J. Biol. Chem. 283 (2008) 15878–15883, https://doi.org/10.1074/jbc.M800731200.

[17] G. Zaccagnini, B. Maimone, V.D. Stefano, P. Fasanaro, S. Greco, A. Perfetti, M. C. Capogrossi, C. Gaetano, F. Martelli, Hypoxia-induced miR-210 modulates tissue response to acute peripheral ischemia, Antioxidants Redox Signal. 21 (2014) 1177–1188, https://doi.org/10.1089/ars.2013.5206.

[18] M. Besnier, S. Gasparino, R. Vono, E. Sangalli, A. Facoetti, V. Bollati, L. Cantone, G. Zaccagnini, B. Maimone, P. Fuschi, et al., miR-210 enhances the therapeutic potential of bone-marrow-derived circulating proangiogenic cells in the setting of limb ischemia, Mol. Ther. : the journal of the American Society of Gene Therapy 26 (2018) 1694–1705. S1525-0016(18)30262-4 [pii].

[19] H.W. Kim, H.K. Haider, S. Jiang, M. Ashraf, Ischemic preconditioning augments survival of stem cells via miR-210 expression by targeting caspase-8-associated protein 2, J. Biol. Chem. 284 (2009) 33161–33168, https://doi.org/10.1074/jbc.M109.020925.

[20] R. Wu, J. Zeng, J. Yuan, X. Deng, Y. Huang, L. Chen, P. Zhang, H. Feng, Z. Liu, Z. Wang, et al., MicroRNA-210 overexpression promotes psoriasis-like inflammation by inducing Th1 and Th17 cell differentiation, J. Clin. Invest. 128 (2018) 2551–2568, https://doi.org/10.1172/JCI97426.

[21] M.Z. Noman, B. Janji, S. Hu, J.C. Wu, F. Martelli, V. Bronte, S. Chouaib, Tumor-promoting effects of myeloid-derived suppressor cells are potentiated by hypoxia-induced expression of miR-210, Cancer Res. 75 (2015) 3771–3787, https://doi.org/10.1158/0008-5472.CAN-15-0405.

[22] J. Qi, Y. Qiao, P. Wang, S. Li, W. Zhao, C. Gao, microRNA-210 negatively regulates LPS-induced production of proinflammatory cytokines by targeting NF-κB1 in murine macrophages, FEBS Lett. 586 (2012) 1201–1207, https://doi.org/10.1016/j.febslet.2012.03.011.

[23] V. Kumar, A. Kumar, S. Das, A. Kumar, K. Abhishek, S. Verma, A. Mandal, R. K. Singh, P. Das, Leishmania donovani activates hypoxia inducible factor-1α and miR-210 for survival in macrophages by downregulation of NF-κB mediated pro-inflammatory immune response, Front. Microbiol. 9 (2018) 385, https://doi.org/10.3389/fmicb.2018.00385.

[24] F. Virga, F. Cappellesso, B. Stijlemans, A.T. Henze, R. Trotta, J.V. Audenaerde, A. S. Mirchandani, M.A. Sanchez-Garcia, J. Vandewalle, F. Orso, et al., Macrophage miR-210 induction and metabolic reprogramming in response to pathogen interaction boost life-threatening inflammation, Sci. Adv. 7 (2021) eabf0466, https://doi.org/10.1126/sciadv.abf0466. Print 2021 May eabf0466 [pii].

[25] G. Zaccagnini, S. Greco, M. Longo, B. Maimone, C. Voellenkle, P. Fuschi, M. Carrara, P. Creo, D. Maselli, M. Tirone, et al., Hypoxia-induced miR-210 modulates the inflammatory response and fibrosis upon acute ischemia, Cell Death Dis. 12 (2021) 435–439, https://doi.org/10.1038/s41419-021-03713-9.

[26] H. Hao, S. Yan, X. Zhao, X. Han, N. Fang, Y. Zhang, C. Dai, W. Li, H. Yu, Y. Gao, et al., Atrial myocyte-derived exosomal microRNA contributes to atrial fibrosis in atrial fibrillation, J. Transl. Med. 20 (2022) 407, https://doi.org/10.1186/s12967-022-03617-y.

[27] V. Bodempudi, P. Hergert, K. Smith, H. Xia, J. Herrera, M. Peterson, W. Khalil, J. Kahm, P.B. Bitterman, C.A. Henke, miR-210 promotes IPF fibroblast proliferation in response to hypoxia, Am. J. Physiol. Lung Cell Mol. Physiol. 307 (2014) L283–L294, https://doi.org/10.1152/ajplung.00069.2014.

[28] H. Røsjø, M.B. Dahl, A. Bye, J. Andreassen, M. Jørgensen, U. Wisløff, G. Christensen, T. Edvardsen, T. Omland, Prognostic value of circulating microRNA-210 levels in patients with moderate to severe aortic stenosis, PLoS One 9 (2014) e91812, https://doi.org/10.1371/journal.pone.0091812.

[29] G. Zaccagnini, B. Maimone, P. Fuschi, D. Maselli, G. Spinetti, C. Gaetano, F. Martelli, Overexpression of miR-210 and its significance in ischemic tissue damage, Sci. Rep. 7 (2017) 9563–9564, https://doi.org/10.1038/s41598-017-09763-4.

[30] P. Hu, D. Zhang, L. Swenson, G. Chakrabarti, E.D. Abel, S.E. Litwin, Minimally invasive aortic banding in mice: effects of altered cardiomyocyte insulin signaling during pressure overload, Am. J. Physiol. Heart Circ. Physiol. 285 (2003) H1261–H1269, https://doi.org/10.1152/ajpheart.00108.2003.

[31] G. Zaccagnini, A. Palmisano, T. Canu, B. Maimone, F.M.L. Russo, F. Ambrogi, C. Gaetano, F.D. Cobelli, A.D. Maschio, A. Esposito, et al., Magnetic resonance imaging allows the evaluation of tissue damage and regeneration in a mouse model of critical limb ischemia, PLoS One 10 (2015) e0142111, https://doi.org/10.1371/journal.pone.0142111.

[32] T.D. Schmittgen, K.J. Livak, Analyzing real-time PCR data by the comparative C(T) method, Nat. Protoc. 3 (2008) 1101–1108.

[33] A. Almazloum, H. Khalil, Isolation of adult mouse cardiac fibroblasts, Current Protocols 3 (2023) e840.

[34] J. Man, P. Barnett, V.M. Christoffels, Structure and function of the nppa-nppb cluster locus during heart development and disease, Cell. Mol. Life Sci. 75 (2018) 1435–1444, https://doi.org/10.1007/s00018-017-2737-0.

[35] A.H. Ellims, L.M. Iles, L. Ling, J.L. Hare, D.M. Kaye, A.J. Taylor, Diffuse myocardial fibrosis in hypertrophic cardiomyopathy can Be identified by cardiovascular magnetic resonance, and is associated with left ventricular diastolic dysfunction, J. Cardiovasc. Magn. Reson. 14 (2012) 76, https://doi.org/10.1186/1532-429X-14-76.
[36] M. Tanaka, H. Fujiwara, T. Onodera, D.J. Wu, Y. Hamashima, C. Kawai, Quantitative analysis of myocardial fibrosis in normals, hypertensive hearts, and hypertrophic cardiomyopathy, Br. Heart J. 55 (1986) 575–581, https://doi.org/10.1136/hrt.55.6.575.
[37] S. Chen, A.F.U.H. Saeed, Q. Liu, Q. Jiang, H. Xu, G.G. Xiao, L. Rao, Y. Duo, Macrophages in immunoregulation and therapeutics, Signal Transduct. Targeted Ther. 8 (2023) 207, https://doi.org/10.1038/s41392-023-01452-1.
[38] U.C. Sharma, S. Pokharel, T.J. van Brakel, J.H. van Berlo, J.P.M. Cleutjens, B. Schroen, S. André, H.J.G.M. Crijns, H.-J. Gabius, J. Maessen, et al., Galectin-3 marks activated macrophages in failure-prone hypertrophied hearts and contributes to cardiac dysfunction, Circulation 110 (2004) 3121–3128, https://doi.org/10.1161/01.CIR.0000147181.65298.4D.
[39] O. Frunza, I. Russo, A. Saxena, A.V. Shinde, C. Humeres, W. Hanif, V. Rai, Y. Su, N. G. Frangogiannis, Myocardial galectin-3 expression is associated with remodeling of the pressure-overloaded heart and may delay the hypertrophic response without affecting survival, dysfunction, and cardiac fibrosis, Am. J. Pathol. 186 (2016) 1114–1127, https://doi.org/10.1016/j.ajpath.2015.12.017.
[40] R.A. de Boer, A.A. Voors, P. Muntendam, W.H. van Gilst, D.J. van Veldhuisen, Galectin-3: a novel mediator of heart failure development and progression, Eur. J. Heart Fail. 11 (2009) 811–817, https://doi.org/10.1093/eurjhf/hfp097.
[41] N.G. Frangogiannis, Galectin-3 in the fibrotic response: cellular targets and molecular mechanisms, Int. J. Cardiol. 258 (2018) 226–227, https://doi.org/10.1016/j.ijcard.2018.01.128.
[42] K. Schimmel, K. Ichimura, S. Reddy, F. Haddad, E. Spiekerkoetter, Cardiac fibrosis in the pressure overloaded left and right ventricle as a therapeutic target, Front. Cardiovasc. Med. 9 (2022) 886553, https://doi.org/10.3389/fcvm.2022.886553.
[43] H. Venugopal, A. Hanna, C. Humeres, N.G. Frangogiannis, Properties and functions of fibroblasts and myofibroblasts in myocardial infarction, Cells 11 (2022), https://doi.org/10.3390/cells11091386.
[44] M.A.A. Mahdy, Skeletal muscle fibrosis: an overview, Cell Tissue Res. 375 (2019) 575–588, https://doi.org/10.1007/s00441-018-2955-2.
[45] M.M. Chen, A. Lam, J.A. Abraham, G.F. Schreiner, A.H. Joly, CTGF expression is induced by tgf- beta in cardiac fibroblasts and cardiac myocytes: a potential role in heart fibrosis, J. Mol. Cell. Cardiol. 32 (2000) 1805–1819, https://doi.org/10.1006/jmcc.2000.1215.
[46] L.E. Dorn, J.M. Petrosino, P. Wright, F. Accornero, CTGF/CCN2 is an autocrine regulator of cardiac fibrosis, J. Mol. Cell. Cardiol. 121 (2018) 205–211, https://doi.org/10.1016/j.yjmcc.2018.07.130.
[47] T.J. Kelly, A.L. Souza, C.B. Clish, P. Puigserver, A hypoxia-induced positive feedback loop promotes hypoxia-inducible factor 1alpha stability through miR-210 suppression of glycerol-3-phosphate dehydrogenase 1-like, Mol. Cell Biol. 31 (2011) 2696–2706, https://doi.org/10.1128/MCB.01242-10.
[48] M.P. Puisségur, N.M. Mazure, T. Bertero, L. Pradelli, S. Grosso, K. Robbe-Sermesant, T. Maurin, K. Lebrigand, B. Cardinaud, V. Hofman, et al., miR-210 is overexpressed in late stages of lung cancer and mediates mitochondrial alterations associated with modulation of HIF-1 activity, Cell Death Differ. 18 (2011) 465–478, https://doi.org/10.1038/cdd.2010.119.
[49] M. Hölscher, K. Schäfer, S. Krull, K. Farhat, A. Hesse, M. Silter, Y. Lin, B.J. Pichler, P. Thistlethwaite, A. El-Armouche, et al., Unfavourable consequences of chronic cardiac HIF-1α stabilization, Cardiovasc. Res. 94 (2012) 77–86, https://doi.org/10.1093/cvr/cvs014.
[50] Y.A. Minamishima, J. Moslehi, N. Bardeesy, D. Cullen, R.T. Bronson, W.G.J. Kaelin, Somatic inactivation of the PHD2 prolyl hydroxylase causes polycythemia and congestive heart failure, Blood 111 (2008) 3236–3244, https://doi.org/10.1182/blood-2007-10-117812.
[51] J. Moslehi, Y.A. Minamishima, J. Shi, D. Neuberg, D.M. Charytan, R.F. Padera, S. Signoretti, R. Liao, W.G.J. Kaelin, Loss of hypoxia-inducible factor prolyl hydroxylase activity in cardiomyocytes phenocopies ischemic cardiomyopathy, Circulation 122 (2010) 1004–1016, https://doi.org/10.1161/CIRCULATIONAHA.109.922427.
[52] J. Krishnan, M. Suter, R. Windak, T. Krebs, A. Felley, C. Montessuit, M. Tokarska-Schlattner, E. Aasum, A. Bogdanova, E. Perriard, et al., Activation of a HIF1alpha-PPARgamma Axis underlies the integration of glycolytic and lipid anabolic pathways in pathologic cardiac hypertrophy, Cell Metabol. 9 (2009) 512–524, https://doi.org/10.1016/j.cmet.2009.05.005.
[53] J.A. Hill, E.N. Olson, Cardiac plasticity, N. Engl. J. Med. 358 (2008) 1370–1380, https://doi.org/10.1056/NEJMra072139.
[54] F.T. Liu, D.K. Hsu, R.I. Zuberi, I. Kuwabara, E.Y. Chi, W.R.J. Henderson, Expression and function of galectin-3, a beta-galactoside-binding lectin, in human monocytes and macrophages, Am. J. Pathol. 147 (1995) 1016–1028.
[55] S. Sato, R.C. Hughes, Regulation of secretion and surface expression of mac-2, a galactoside-binding protein of macrophages, J. Biol. Chem. 269 (1994) 4424–4430.
[56] L. Yu, W.P.T. Ruifrok, M. Meissner, E.M. Bos, H. van Goor, B. Sanjabi, P. van der Harst, B. Pitt, I.J. Goldstein, J.A. Koerts, et al., Genetic and pharmacological inhibition of galectin-3 prevents cardiac remodeling by interfering with myocardial fibrogenesis, Circ Heart Fail 6 (2013) 107–117, https://doi.org/10.1161/CIRCHEARTFAILURE.112.971168.
[57] G. Zaccagnini, S. Greco, C. Voellenkle, C. Gaetano, F. Martelli, miR-210 hypoxamiR in Angiogenesis and Diabetes, Antioxidants Redox Signal. 36 (2022) 685–706, https://doi.org/10.1089/ars.2021.0200.
[58] Y.-L. Lou, F. Guo, F. Liu, F.-L. Gao, P.-Q. Zhang, X. Niu, S.-C. Guo, J.-H. Yin, Y. Wang, Z.-F. Deng, miR-210 activates notch signaling pathway in angiogenesis induced by cerebral ischemia, Mol. Cell. Biochem. 370 (2012) 45–51, https://doi.org/10.1007/s11010-012-1396-6.
[59] F. Xiao, H. Qiu, L. Zhou, X. Shen, L. Yang, K. Ding, WSS25 inhibits dicer, downregulating microRNA-210, which targets ephrin-A3, to suppress human microvascular endothelial cell (HMEC-1) tube formation, Glycobiology 23 (2013) 524–535, https://doi.org/10.1093/glycob/cwt004.
[60] L. Zeng, X. He, Y. Wang, Y. Tang, C. Zheng, H. Cai, J. Liu, Y. Wang, Y. Fu, G. Y. Yang, MicroRNA-210 overexpression induces angiogenesis and neurogenesis in the normal adult mouse brain, Gene Ther. 21 (2014) 37–43, https://doi.org/10.1038/gt.2013.55.
[61] S. Narayanan, S.E. Angelstig, C. Xu, J. Grünler, A. Zhao, W. Zhu, N.X. Landén, M. Ståhle, J. Zhang, M. Ivan, et al., HypoxamiR-210 accelerates wound healing in diabetic mice by improving cellular metabolism, Commun. Biol. 3 (2020), https://doi.org/10.1038/s42003-020-01495-y, 768-y.
[62] B.W. Wong, E. Marsch, L. Treps, M. Baes, P. Carmeliet, Endothelial cell metabolism in Health and disease: impact of hypoxia, EMBO J. 36 (2017) 2187–2203, https://doi.org/10.15252/embj.201696150.
[63] E.A. Osuma, D.W. Riggs, A.A. Gibb, B.G. Hill, High throughput measurement of metabolism in planarians reveals activation of glycolysis during regeneration, Regeneration 5 (2018) 78–86, https://doi.org/10.1002/reg2.95.
[64] T. Shoji, T. Nakasa, K. Yamasaki, A. Kodama, S. Miyaki, T. Niimoto, A. Okuhara, N. Kamei, N. Adachi, M. Ochi, The effect of intra-articular injection of microRNA-210 on ligament healing in a rat model, Am. J. Sports Med. 40 (2012) 2470–2478, https://doi.org/10.1177/0363546512458894.
[65] Y. Kawanishi, T. Nakasa, T. Shoji, M. Hamanishi, R. Shimizu, N. Kamei, M. A. Usman, M. Ochi, Intra-articular injection of synthetic microRNA-210 accelerates avascular meniscal healing in rat medial meniscal injured model, Arthritis Res. Ther. 16 (2014) 488, https://doi.org/10.1186/s13075-014-0488-y.
[66] S.Y. Chan, J. Loscalzo, MicroRNA-210: a unique and pleiotropic hypoxamir, Cell Cycle 9 (2010) 1072–1083, doi:11006 [pii].
[67] M. Ivan, A.L. Harris, F. Martelli, R. Kulshreshtha, Hypoxia response and microRNAs: No longer two separate worlds, J. Cell Mol. Med. 12 (2008) 1426–1431, https://doi.org/10.1111/j.1582-4934.2008.00398.x.
[68] M.L. Marcus, S. Koyanagi, D.G. Harrison, D.B. Doty, L.F. Hiratzka, C.L. Eastham, Abnormalities in the coronary circulation that occur as a consequence of cardiac hypertrophy, Am. J. Med. 75 (1983) 62–66, https://doi.org/10.1016/0002-9343(83)90120-1.
[69] A. Xiong, Y. Liu, Targeting hypoxia inducible factors-1α as a novel therapy in fibrosis, Front. Pharmacol. 8 (2017) 326, https://doi.org/10.3389/fphar.2017.00326.